



HAL
open science

Constructing “Li-rich Ni-rich” oxide cathodes for high-energy-density Li-ion batteries

Biao Li, Gwenaëlle Rousse, Leiting Zhang, Maxim Avdeev, Michaël Deschamps, Artem Abakumov, Jean-Marie Tarascon

► **To cite this version:**

Biao Li, Gwenaëlle Rousse, Leiting Zhang, Maxim Avdeev, Michaël Deschamps, et al.. Constructing “Li-rich Ni-rich” oxide cathodes for high-energy-density Li-ion batteries. *Energy & Environmental Science*, 2023, 16 (3), pp.1210-1222. 10.1039/D2EE03969A . hal-04047592v1

HAL Id: hal-04047592

<https://hal.science/hal-04047592v1>

Submitted on 27 Mar 2023 (v1), last revised 7 Apr 2023 (v2)

HAL is a multi-disciplinary open access archive for the deposit and dissemination of scientific research documents, whether they are published or not. The documents may come from teaching and research institutions in France or abroad, or from public or private research centers.

L'archive ouverte pluridisciplinaire **HAL**, est destinée au dépôt et à la diffusion de documents scientifiques de niveau recherche, publiés ou non, émanant des établissements d'enseignement et de recherche français ou étrangers, des laboratoires publics ou privés.

1 Constructing “Li-rich Ni-rich” oxide cathodes for high-energy-density Li-ion 2 batteries

3 Biao Li^{1,2}, Gwenaëlle Rousse^{1,2,3}, Leiting Zhang⁴, Maxim Avdeev^{5,6}, Michaël Deschamps^{2,7}, Artem M.
4 Abakumov⁸, Jean-Marie Tarascon^{1,2,3*}

5 ¹Chimie du Solide-Energie, UMR 8260, Collège de France, 75231 Paris Cedex 05, France.

6 ²Réseau sur le Stockage Electrochimique de l’Energie (RS2E), FR CNRS 3459, France.

7 ³Sorbonne Université, 4 Place Jussieu, 75005, Paris, France.

8 ⁴Battery Electrodes and Cells, Electrochemistry Laboratory, Paul Scherrer Institute, Forschungsstrasse 111, 5232
9 Villigen-PSI, Switzerland. (*Present address: Department of Chemistry – Ångström Laboratory, Uppsala University,*
10 *Box 538, SE-751 21 Uppsala, Sweden.*)

11 ⁵School of Chemistry, The University of Sydney, Sydney, New South Wales, Australia.

12 ⁶Australian Centre for Neutron Scattering, Australian Nuclear Science and Technology Organisation, Kirrawee DC,
13 New South Wales, Australia.

14 ⁷CNRS, CEMHTI UPR3079, Université d’Orléans, Orléans, France

15 ⁸Center for Energy Science and Technology, Skolkovo Institute of Science and Technology, Nobel str. 3, 121205
16 Moscow, Russia.

17 * Corresponding author: jean-marie.tarascon@college-de-france.fr

18 **Key words:** Li-ion batteries, Li-rich, Ni-rich, layered, disordered

19

20 Abstract

21 The current exploration of high-energy-density cathode materials for Li-ion batteries is mainly
22 concentrated on either so-called “Li-rich” or “Ni-rich” oxides. However, both are suffering from
23 formidable practical challenges. Here, we combine these two concepts to obtain “Li-rich Ni-rich”
24 oxides in pursuit of more practical high-energy-density cathodes. As a proof of concept, we
25 synthesized an array of $\text{Li}_{1+y}\text{Ni}_{(3-5y)/3}\text{Mo}_{2y/3}\text{O}_2$ oxides, whose structures were identified to be the
26 coexistence of LiNiO_2 -rich and Li_4MoO_5 -rich domains with the aid of XRD, TEM, and NMR
27 techniques. Such intergrowth structure with 5-20 nm in size enables excellent mechanical and
28 structural reversibility for the layered rock-salt LiNiO_2 -rich domain upon cycling thanks to the
29 robust cubic rock-salt Li_4MoO_5 -rich domain enabling an “epitaxial stabilization” effect. As a
30 result, we achieved high capacities ($>220 \text{ mA h g}^{-1}$) with Ni contents as low as 80%; the
31 $\text{Li}_{1.09}\text{Ni}_{0.85}\text{Mo}_{0.06}\text{O}_2$ member ($y = 0.09$) shows much improved cycling performances (91%
32 capacity retention for 100 cycles at C/10) compared with pure LiNiO_2 . This work validates the
33 feasibility of constructing Li-rich Ni-rich compounds in a form of intergrowing domains and
34 hence unlocks vast possibilities for future cathode design.

35

36 Introduction

37 The electric vehicles (EVs) market is under rapid growth, as witnessed by the number of
38 EVs on the roads that has set a new record (>10 millions) at the end of 2020¹. The prosperity of
39 the EV market is driving the demand for high-energy-density Li-ion batteries acting as power
40 sources. Throughout the past decades, enormous efforts have been devoted to exploring potential
41 candidates for both cathodes and anodes in pursuit of higher energy densities. Among them,
42 classical cathode candidates, such as LiCoO_2 , LiFePO_4 , and $\text{LiNi}_{1/3}\text{Co}_{1/3}\text{Mn}_{1/3}\text{O}_2$, primarily
43 suffer from low capacities, typically below 200 mA h g^{-1} and, therefore, low energy densities.²
44 Hence, practical high-energy-density electrodes are pressingly demanded.

45 The current exploration of high-energy-density cathode materials is ongoing along two
46 routes. The first concerns the so-called Li-rich materials, $\text{Li}_{1+x}\text{M}_{1-x}\text{O}_2$ (M denotes transition metal
47 hereafter), with additional Li ions partially replacing M ions at the transition metal layer.³ They
48 can provide exceptionally high capacities ($>250 \text{ mA h g}^{-1}$) stemming from anionic redox
49 phenomenon, a paradigm-shift concept that is receiving worldwide attentions⁴⁻⁷. However, this
50 class of materials are plagued by their common shortcomings such as voltage hysteresis and
51 voltage fade brought forward by the aforementioned anionic redox, and their prospect of
52 practical use remains unclear unless these bottlenecks are overcome^{4,8}.

53 In parallel, the community is also striving on another strategy — the so-called Ni-rich (or
54 high-Ni) oxides with either the $\text{LiNi}_x\text{Co}_y\text{Mn}_{1-x-y}\text{O}_2$ (NMC) or $\text{LiNi}_x\text{Co}_y\text{Al}_{1-x-y}\text{O}_2$ (NCA)
55 compositions with x typically equal or larger than 0.8.^{9,10} They are derived from LiNiO_2 and are
56 generating great interest owing to their high capacities ($> 200 \text{ mA h g}^{-1}$) and high working
57 potentials ($\sim 3.8 \text{ V}$). However, these Ni-rich electrodes are suffering from mechanical,
58 electrochemical and thermal stability issues that, in some extent, limit their commercial use.¹¹
59 Therefore, our society is in dire need of new strategies for circumventing such weaknesses while
60 keeping or even increasing the cathode capacity.

61 In this work, we aim to explore the feasibility of merging the Li-rich concept into the Ni-
62 rich oxide materials as a potential solution of the dilemma mentioned above. This idea was
63 initiated by the fact that placing additional Li ions in Ni layer should create O 2p non-bonding
64 states that can serve as an additional redox reservoir, which can buffer the electron depletion
65 from σ -type $\text{Ni}(3d)\text{-O}(2p)$ hybridized states that was supposed to cause the devastation of
66 oxygen framework.¹²⁻¹⁴ Besides, the replacement of Ni by Li will also increase the theoretical

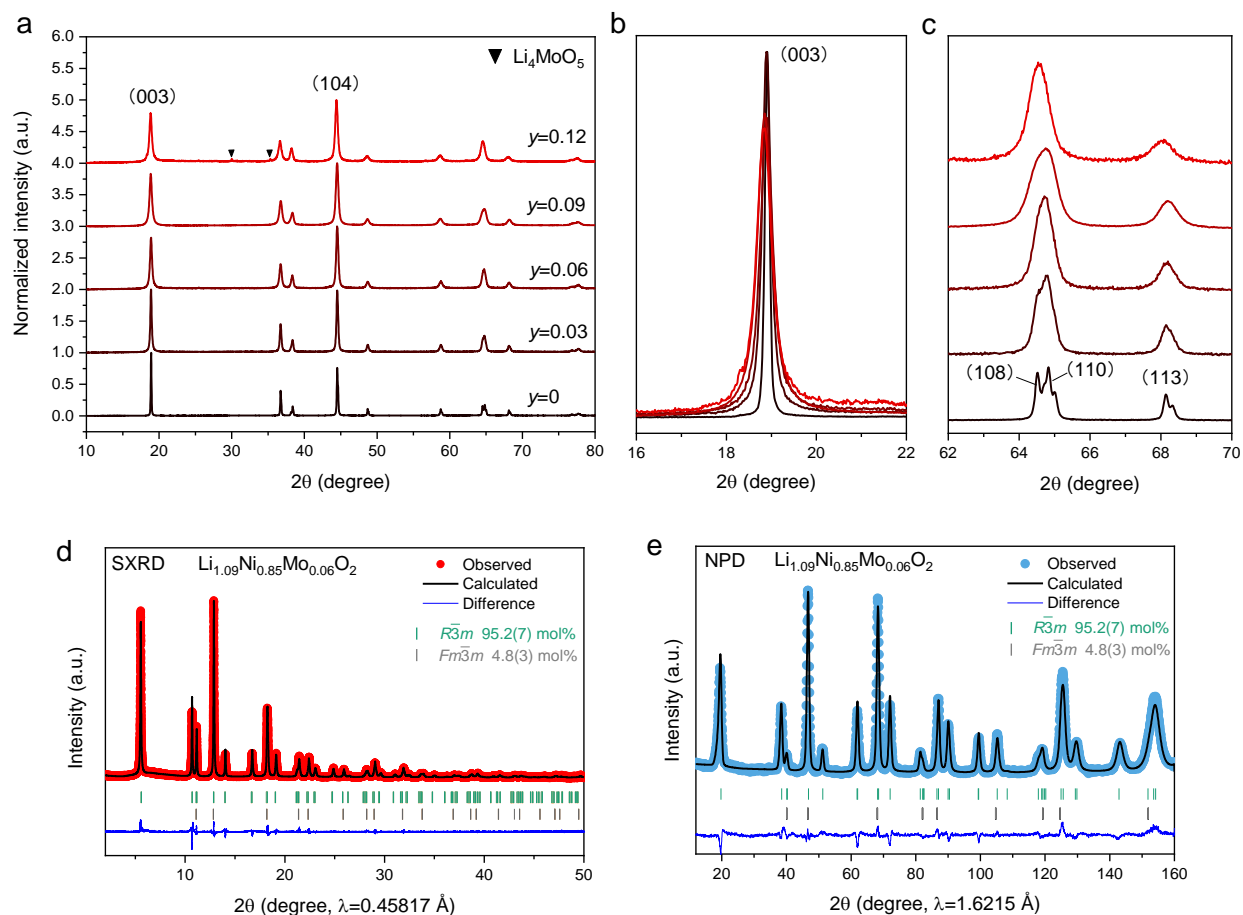
67 capacity and reduce the Ni content in order to get rid of the stability issues. As Li^+ is less
68 positively charged than Ni^{3+} , such design strategy implies the need to introduce another high-
69 valence metal ion, such as Mo^{6+} , W^{6+} , Nb^{5+} , and Mn^{4+} , to balance the charge. The introduction of
70 these redox inactive metal ions can also benefit the stabilization of the structure, as frequently
71 suggested by previous works¹⁵⁻¹⁷.

72 We herein implement this strategy by placing additional Li^+ and Mo^{6+} ions, as a proof of
73 concept, into LiNiO_2 , to generate an array of Li-rich Ni-rich materials that can be nominally
74 formulated as $\text{Li}_{1+y}\text{Ni}_{(3-5y)/3}\text{Mo}_{2y/3}\text{O}_2$ ($y=0.03, 0.06, 0.09, \text{ and } 0.12$). We found that these materials,
75 instead of forming solid solutions, are composed of layered LiNiO_2 -based domains and
76 Li_4MoO_5 -based disordered rock-salt domains intergrown together, as evidenced by synchrotron
77 X-ray powder diffraction (SXRD), neutron powder diffraction (NPD), transmission electron
78 microscopy (TEM) and nuclear magnetic resonance (NMR) studies. As a result, these Li-rich Ni-
79 rich composites show comparable and even higher capacities ($210\sim 230 \text{ mA h g}^{-1}$), even with Ni
80 contents as low as 80%, compared with that of pure LiNiO_2 (220 mA h g^{-1}), with some of them
81 showing excellent cycling stabilities as well.

82

83 **Results and discussions**

84 **General structural characterizations.** $\text{Li}_{1+y}\text{Ni}_{(3-5y)/3}\text{Mo}_{2y/3}\text{O}_2$ ($y=0.03, 0.06, 0.09, \text{ and } 0.12$)
85 were synthesized via a solution-preceded solid-state process (the details can be found in the
86 experimental section). The elemental compositions were checked by inductively coupled plasma
87 atomic emission spectroscopy (ICP-AES), showing Li/Ni ratios consistent with the nominal ones
88 (Table S1). However, Mo contents were found to be far below the theoretical values, which is
89 due to the Mo oxides (e.g. MoO_3) have limited solubility in acidic media especially when aqua
90 regia was used for ICP-AES measurements¹⁸. Scanning electron microscopy (SEM) coupled with
91 energy dispersive X-ray analysis (EDX) was further employed to validate the Ni/Mo ratios, as
92 tabulated in Table S2, showing good consistency with the nominal values.

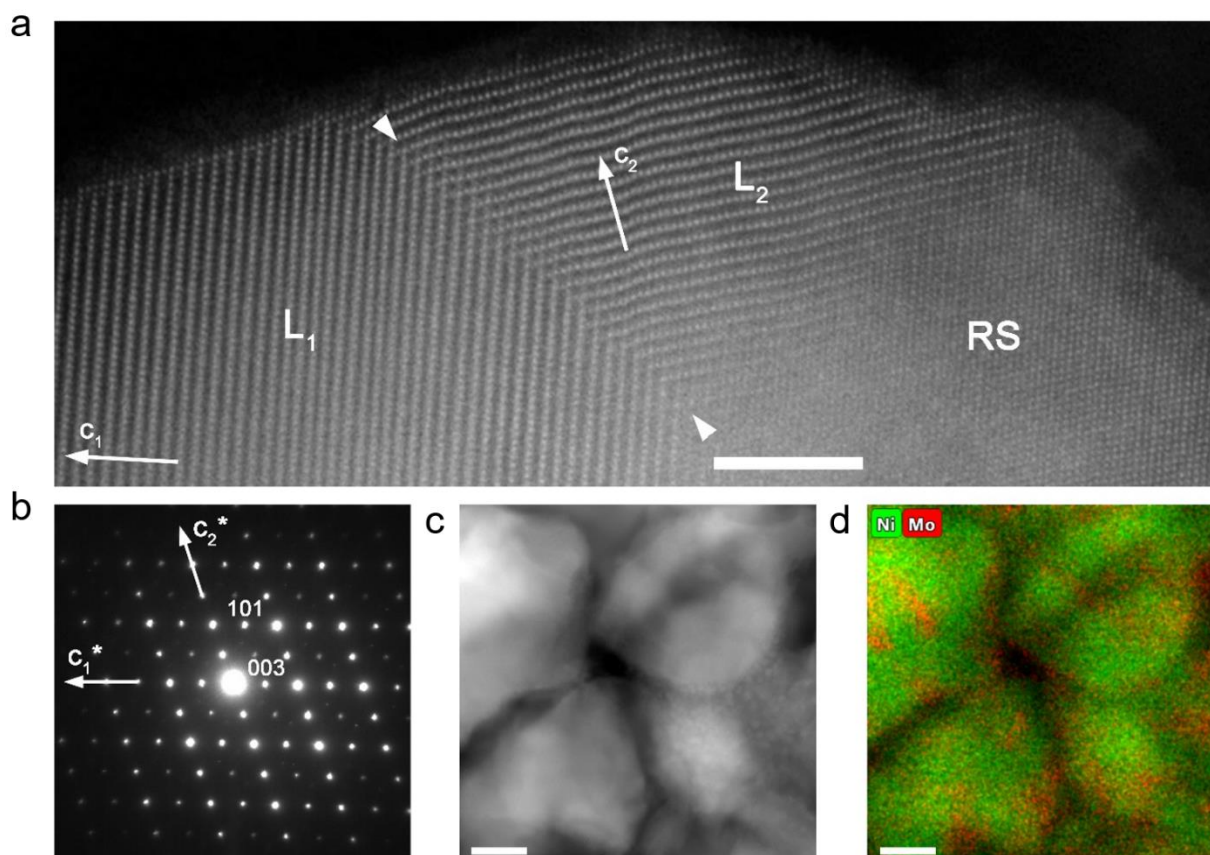


93

94 **Figure 1. Structural characterizations of $\text{Li}_{1+y}\text{Ni}_{(3-5y)/3}\text{Mo}_{2y/3}\text{O}_2$ ($y=0, 0.03, 0.06, 0.09, 0.12$).** (a) XRD
 95 patterns. (b)(c) Enlarged parts of XRD patterns. (d)(e) Combined Rietveld refinement results of SXRDP
 96 and NPD for the $y=0.09$ member ($\text{Li}_{1.09}\text{Ni}_{0.85}\text{Mo}_{0.06}\text{O}_2$). The refinement was done with a two-phase model
 97 with $\text{Li}_{1.04}\text{Ni}_{0.93}\text{Mo}_{0.03}\text{O}_2$ ($R\bar{3}m$) and Li_4MoO_5 ($Fm\bar{3}m$) whose molar percentage was indicated. The color-
 98 coded vertical bars are the Bragg positions of each phase.

99 X-ray powder diffraction (XRD) was further employed to investigate the structures of the
 100 as-synthesized $\text{Li}_{1+y}\text{Ni}_{(3-5y)/3}\text{Mo}_{2y/3}\text{O}_2$ samples. As shown in Fig. 1a, LiNiO_2 is well crystallized in
 101 a typical layered structure with $R\bar{3}m$ symmetry in line with what has been reported previously¹⁹.
 102 Upon the addition of Li and Mo, the diffraction peaks are getting broader as observed from the
 103 evolution of (003) peak (Fig. 1b) and (108), (110) peaks (Fig. 1c). This indicates a decrease of
 104 the crystallite sizes, as identified by the SEM images (Fig. S1), with probably also an increasing
 105 degree of the micro-strain. Besides, the lattice parameter a and c , obtained via Rietveld
 106 refinement, generally increase as a function of Li content (Fig. S2). Such lattice expansion
 107 suggests the successful incorporation into the LiNiO_2 lattice of additional Li^+ ions, the ionic
 108 radius of which ($\sim 0.76\text{\AA}$) is larger than that of Ni^{3+} ($\sim 0.56\text{\AA}$). In addition, the most prominent

109 change is observed for the (003) peak intensity, which gradually decreases relative to that of the
 110 (104) peak upon Li and Mo addition (Fig. 1a). Considering that the (003)/(104) peak intensity
 111 ratio is widely used to gauge the degree of cation mixing between the Li and M layers, we
 112 presumed that its decrease is a signature of the higher degree of cation mixing occurring upon Li
 113 and Mo incorporation.



114
 115 **Figure 2. TEM analysis of $\text{Li}_{1.09}\text{Ni}_{0.85}\text{Mo}_{0.06}\text{O}_2$.** (a) HAADF-STEM image showing the twinned domains
 116 of the layered $R\text{-}3m$ structure (L_1 and L_2) along with a disordered rock-salt (RS) domain. The orientation
 117 of the c -axis in the layered domains is marked with arrows. The (104) twin plane is traced with
 118 arrowheads. The scale bar is 5 nm. (b) ED pattern demonstrating the twinned layered O3-type structure.
 119 The reciprocal lattice axes c^* for the twinned domains are marked. (c) HAADF-STEM image and (d) the
 120 color-coded EDX map demonstrating the mosaic Ni (green) and Mo (red) distribution. The scale bar is 20
 121 nm.

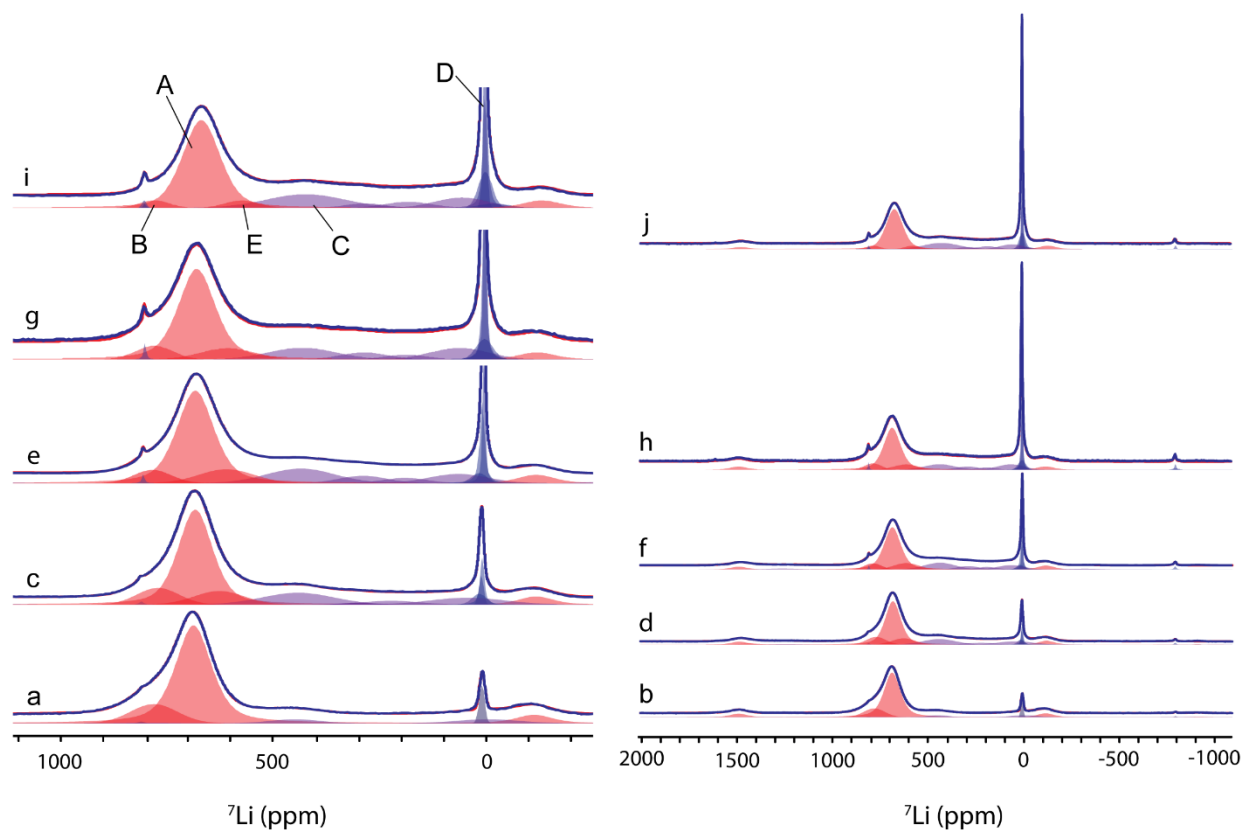
122 **TEM analysis.** Surprisingly, TEM images of the $\text{Li}_{1.09}\text{Ni}_{0.85}\text{Mo}_{0.06}\text{O}_2$ sample showed a
 123 two-phase intergrowth system rather than a solid solution. As shown in Fig. 2a,b, the high-angle
 124 annular dark-field scanning transmission electron microscopy (HAADF-STEM) image and
 125 electron diffraction (ED) pattern reveal that the O3 structure is split into twinned nanodomains
 126 separated by twin planes (marked with arrowheads in Fig. 2a; the detailed indexing of the ED

127 pattern is provided in Fig.S3). The transition metals and Li cations in these domains are well
128 ordered as no HAADF intensity is observed between the brightest dots of the M columns. This
129 indicates low fractions of Ni and Mo in the octahedral Li sites. The apparent cationic disorder in
130 these domains is observed in the very surface layer (i.e. the thickness of one unit cell). However,
131 next to the well-ordered layered structure, rock-salt-type disordered domains were also found,
132 displaying a mixed distribution of the M and Li cations (marked as RS in Fig. 2a). Such a
133 structural inhomogeneity apparently coexists with a chemical inhomogeneity as unequivocally
134 observed from the energy dispersive X-ray (EDX) elemental mapping (Fig. 2c,d). It clearly
135 shows a mosaic-like Mo and Ni distribution pointing toward the coexistence of a Ni-rich phase
136 and a Mo-rich phase. The Ni:Mo atomic ratio quantified with the EDX spectra integrated over
137 large areas (c.a. 200×200 nm) amounts to 93.3(6):6.7(6) that corresponds to $y = 0.09$, in
138 agreement with the bulk composition of the sample determined from ICP. The Ni:Mo =
139 97.2(5):2.8(5) atomic ratio was measured for the Ni-rich phase that corresponds to $y = 0.04$ and
140 hence a composition close to $\text{Li}_{1.04}\text{Ni}_{0.93}\text{Mo}_{0.03}\text{O}_2$. The domains of the Mo-rich phase are too
141 small and overlap heavily with the Ni-rich phase, so their composition cannot be reliably
142 determined.

143
144 **NMR analysis.** To explore the exact chemical structure of these intergrown phases, ^7Li NMR
145 spectroscopy was also used as it is an excellent probe of the paramagnetic ions around lithium
146 spins, providing access to their oxidation state and their connectivity to the observed lithium spin.

147 For typical Ni-based layered oxides, several Li environments can be distinguished by ^7Li
148 NMR depending on the number and position of Ni ions interacting through Ni-O-Li bonds. As
149 calculated in a lithium nickel cobalt oxide, each Ni^{3+} is expected to contribute to the ^7Li shift by
150 adding -15 ppm in an edge-sharing position (Li-O-Ni angle at 90°), and +110 ppm in a corner
151 sharing position (Li-O-Ni angle of 180°).²⁰⁻²² Those values are found to be -30 and +170 ppm for
152 Ni^{2+} .²³ Diamagnetic ions, such as Li^+ , Mo^{6+} ($4d^0$ ion) and Co^{4+} ($3d^6$ low-spin) are expected to
153 induce minor shift changes. These contributions would give rise to a shift of 570 ppm for a
154 typical layered LiNiO_2 compound (6 $\text{Li}^+\text{-O-Ni}^{3+}$ at 90° and 6 $\text{Li}^+\text{-O-Ni}^{3+}$ at 180°). Nevertheless,
155 in our case, the main LiNiO_2 peak was found at around 680 ppm (peak A in Fig. 3a), a value
156 close to those previously measured^{22,24,25} but slightly larger than the calculated one. The
157 discrepancy may stem from the local distortion arising around the Ni ions (Jahn-Teller) which

158 was absent from the structure used for the calculations. By further deconvolution of the NMR
 159 spectra, we also found an extra peak on the left-hand side of the LiNiO_2 contribution (760-780
 160 ppm, peak B in Fig. 3) in all the samples. This peak can be assigned to the presence of Ni^{2+} ions
 161 (as in $\text{Li}_{1-z}\text{Ni}_{1+z}\text{O}_2$), which usually gives rise to larger shifts, and was also detected in a previous
 162 publication²¹ in which ^6Li MAS NMR showed a similar shoulder appearing on the left-hand side
 163 of the main peak correlating with Ni^{2+} . Interestingly, this peak (B) decreases upon Mo^{6+} addition
 164 (Fig. 3), starting at 13.4% of the total for pristine LiNiO_2 , down to 4-5% for $y=0.09$ and $y=0.12$
 165 members.



166
 167 **Figure 3.** ^7Li MAS-NMR spectra of (a)(b) pristine LiNiO_2 , (c)(d) $\text{Li}_{1.03}\text{Ni}_{0.95}\text{Mo}_{0.02}\text{O}_2$, (e)(f)
 168 $\text{Li}_{1.06}\text{Ni}_{0.9}\text{Mo}_{0.04}\text{O}_2$, (g)(h) $\text{Li}_{1.09}\text{Ni}_{0.85}\text{Mo}_{0.06}\text{O}_2$, and (i)(j) $\text{Li}_{1.12}\text{Ni}_{0.8}\text{Mo}_{0.08}\text{O}_2$. The NMR spectra on the left
 169 hand side show the center region of the spectrum and the diamagnetic contribution (in blue) around 0 ppm
 170 is truncated. The full spectra are shown on the right hand side to illustrate the relative contributions of the
 171 diamagnetic components. The detailed results of the fits are shown in the Table S8. Different species are
 172 labelled with A, B, C, D and E corresponding to the Li signal of LiNiO_2 -rich phase, Ni^{2+} species (like in
 173 $\text{Li}_{1-z}\text{Ni}_{1+z}\text{O}_2$), Ni-rich rock salt phase, diamagnetic Li_4MoO_5 -rich phase, and less Mo^{6+} surrounded Li
 174 species, respectively.

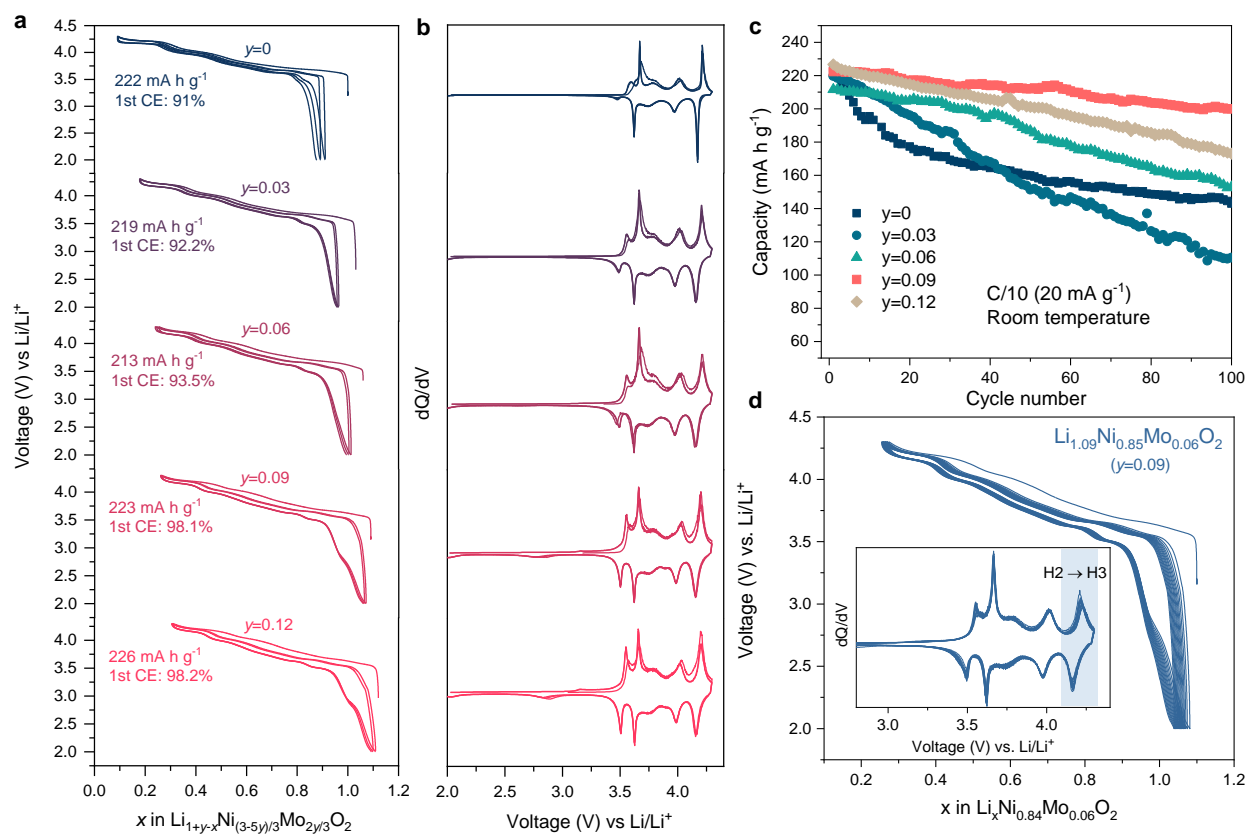
175 Mo^{6+} is a d^0 diamagnetic ion, and therefore, its contribution to the shift of neighboring
 176 ^7Li spins is expected to be negligible compared to Ni^{2+} and Ni^{3+} ions. The presence of a

177 diamagnetic contribution (around 0 ppm, 7.9% of all lithium ions) in pristine LiNiO₂ usually
178 stems from impurities originating from the synthesis process, i.e. lithium hydroxide or carbonate,
179 as seen in numerous previous studies^{21,24,26}. On the other hand, an increasing diamagnetic
180 contribution (peak D around 0 ppm in Fig. 3) that is correlated with molybdenum concentration
181 points towards the creation of diamagnetic molybdenum and lithium-rich domains. This is
182 confirmed by the ⁷Li T₁-relaxation behavior of this diamagnetic part, which displays long T₁
183 constants (≈ 1 s) compared to the T₁ of ⁷Li in the paramagnetic phase (2-5 ms), indicating that
184 those lithium ions are far away from Ni²⁺ or Ni³⁺ ions. Considering the stoichiometry of the
185 diamagnetic domains, one could expect a Li/Mo ratio of 4 in this phase, pointing towards
186 Li₄MoO₅ composition. In such a case, the proportion of lithium belonging to this phase is
187 expected to be 7.8%, 15.1%, 22.0% and 28.6% for y=0.03, 0.06, 0.09 and 0.12 samples,
188 respectively, in good consistency with experimental ones (7.1%, 12.6%, 21.1%, and 24.1%) of
189 the ⁷Li spins that belong to the diamagnetic domains (Table S7). The slightly less lithium than
190 expected is not surprising, since we neglected the interface between the two domains where a
191 Ni/Mo concentration gradient, instead of a very clear transition between the two domains, should
192 exist. Moreover, according to EDX analysis small amount of Mo⁶⁺ is also present in the LiNiO₂
193 domains where some lithium ions have at least one Mo⁶⁺ as second neighbor. In both cases, new
194 environments with intermediary shifts are created, as shown in the NMR spectra (0-400 ppm in
195 Fig. 3), where several unassigned contributions are detected between the contribution of LiNiO₂
196 at 680 ppm and the diamagnetic part around 0 ppm. These peaks are referred to as “LiNi_xMo_{1-x}”
197 species in Table S8. Based on the area ratios between bulk signal of Li₄MoO₅ and interface
198 signal, we further quantified the Li₄MoO₅ domain sizes to be around 3.2, 4.1, 6.0 and 7.3 nm for
199 Li_{1+y}Ni_{(3-5y)/3}Mo_{2y/3}O₂ (y=0.03, 0.06, 0.09, 0.12), respectively, as detailed in Supplementary note I.
200 The domain size of Li_{1.09}Ni_{0.85}Mo_{0.06}O₂ is generally consistent with what we observed from
201 STEM-EDX images in Fig. 2.

202 On the other hand, the detection of peaks on the right-hand side of LiNiO₂ (600-400 ppm),
203 labelled as C and E in Fig.3 and Table S7, seem to indicate lithium ions which have one or two
204 Mo⁶⁺ in their second coordination sphere and therefore provide more shift than lithium ions at
205 the interface of the diamagnetic domains. Such a behavior concerns 14-20% of all lithium ions,
206 and implies the existence of certain amount of Mo ions doped in the LiNiO₂ phase as proved by

207 TEM-EDX, or there is a slow transition (concentration gradient) between Li_4MoO_5 and LiNiO_2
 208 domains.

209 Combining TEM with NMR results, it is clear that the exact structure of
 210 $\text{Li}_{1.09}\text{Ni}_{0.85}\text{Mo}_{0.06}\text{O}_2$ consists of a layered LiNiO_2 -rich phase and a disordered Li_4MoO_5 -rich
 211 phase. In this situation, we can now fully understand the intensity reversal of (003) and (104)
 212 diffraction peaks in XRD (Fig. 1) because of this layered-disordered intergrowth. We further
 213 used a simplified two-phase model ($R\bar{3}m$ $\text{Li}_{1.04}\text{Ni}_{0.93}\text{Mo}_{0.03}\text{O}_2$ and $Fm\bar{3}m$ Li_4MoO_5) to perform
 214 the combined refinement of the collected SXRD and NPD patterns of $\text{Li}_{1.09}\text{Ni}_{0.85}\text{Mo}_{0.06}\text{O}_2$
 215 ($y=0.09$). As shown in Fig. 1d-e and Table S3, the refinement gave satisfying results, providing a
 216 molar ratio of 95.2(7)%:4.8(3)% for the two phases (equivalent to a composition of
 217 $\sim\text{Li}_{1.1}\text{Ni}_{0.83}\text{Mo}_{0.07}\text{O}_2$), in good consistency with the ICP-determined one.



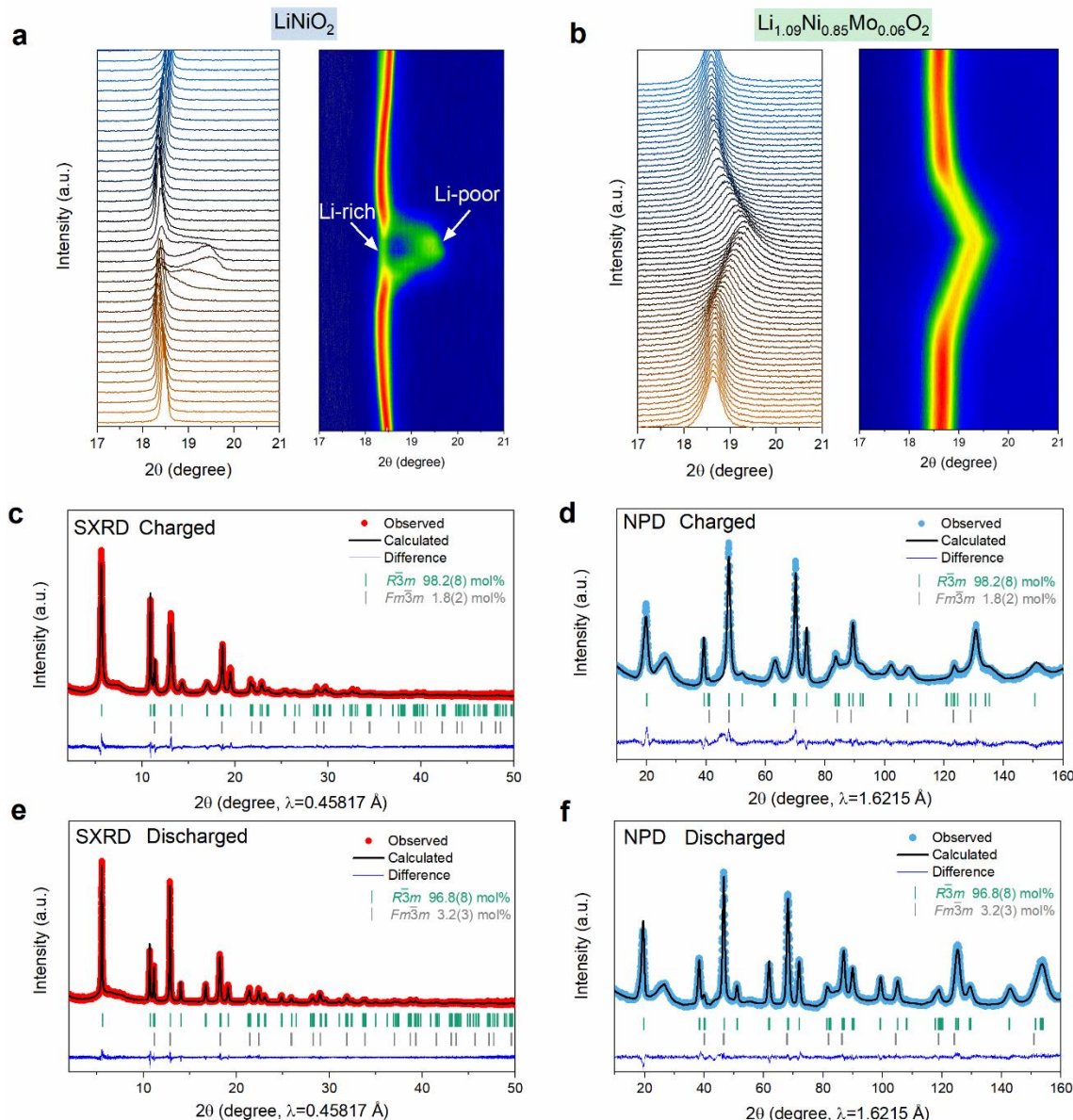
218
 219 **Figure 4. Electrochemistry of $\text{Li}_{1+y}\text{Ni}_{(3-5y)/3}\text{Mo}_{2y/3}\text{O}_2$ ($y=0, 0.03, 0.06, 0.09, 0.12$).** (a) First three cycles
 220 of $\text{Li}_{1+y}\text{Ni}_{(3-5y)/3}\text{Mo}_{2y/3}\text{O}_2$, with their first discharge capacity and first-cycle Coulomb efficiency being
 221 noted. (b) Corresponding dQ/dV plots. (c) Cycling performance of $\text{Li}_{1+y}\text{Ni}_{(3-5y)/3}\text{Mo}_{2y/3}\text{O}_2$. For $y=0.09$
 222 sample, 3 cells data (in light red) are shown together with average capacity and standard deviation (std.)
 223 reported (as shown by the error bar). (d) Cycling curve of $\text{Li}_{1.09}\text{Ni}_{0.85}\text{Mo}_{0.06}\text{O}_2$ with the dQ/dV plots shown
 224 as inset.

225 **Electrochemistry.** A remaining doubt regards if the disordered rock-salt domain is
226 Li_4MoO_5 -rich phase or $\text{Li}_{1-z}\text{Ni}_{1+z}\text{O}_2$ ($z>0.38$) structure; the latter is well-known to be cation-
227 disordered due to the similar ionic radius between Li^+ (0.76\AA) and Ni^{2+} (0.69\AA)^{19,21}. Therefore,
228 one may consider the possibility of $\text{Li}_{1-z}\text{Ni}_{1+z}\text{O}_2$ formation upon the introduction of lithium-
229 consumable Mo^{6+} (in forming Li_4MoO_5) that deprives the Li ions in LiNiO_2 . However, this
230 scenario can hardly happen in our case as we simultaneously put additional Li together with Mo
231 into the structure; as a result, the composition can be written as $\delta\text{LiNiO}_2\cdot(1-\delta)\text{Li}_4\text{MoO}_5$. Indeed,
232 NMR results even show the decrease of $\text{Li}_{1-z}\text{Ni}_{1+z}\text{O}_2$ species (peak B in Fig. 3) upon the increase
233 of Mo concentration.

234 Besides, the electrochemical response also provides crucial implications on the real
235 structures of these electrodes. As shown in Fig.4a, the electrochemical curves for all the samples
236 show similar wavy characteristics with several small plateaus indicative of typical phase
237 transitions in LiNiO_2 -based compounds. These phase transition behaviors can be more
238 unambiguously observed from the sharp peaks in corresponding dQ/dV profiles in Fig. 4b. One
239 specific feature worth mentioning is the sharpness of these dQ/dV peaks does not evolve too
240 much even with decreasing Ni content. This is in stark contrast to archetypical NMC compounds,
241 in which the Mn/Co substitution in LiNiO_2 dramatically smooths the curves and broadens the
242 dQ/dV peaks.²⁷ This unusual feature matches well with the behavior expected for a two-phase
243 system rather than solid solutions, as the former can largely maintain the LiNiO_2 characteristics
244 even with increasing the Mo content. Therefore, the domain with a disordered rock-salt structure
245 is unlikely to be the $\text{Li}_{1-z}\text{Ni}_{1+z}\text{O}_2$ ($z>0.38$) phase, as it normally appears with smoother
246 charge/discharge curves due to the “pillar” effect of Ni^{2+} in Li layer that restrains the layer
247 gliding and hence the phase transitions¹⁹.

248 To further validate the analysis above, non-Li-rich Li-Ni-Mo-O phases were also
249 synthesized, namely, $\text{LiNi}_{1-y}\text{Mo}_y\text{O}_2$ ($y=0.02, 0.04, 0.06, \text{ and } 0.08$), for comparison. As shown in
250 Fig. S4a-d, they show similar behavior for the XRD pattern evolution — the ratio of (003)/(104)
251 peak intensity decreases upon increasing the Mo content, though in a severer manner. However,
252 compared to the Li-rich phases, they exhibit smoothed charge-discharge curves with much
253 broader dQ/dV profiles (Fig. S4e-i). This, as has been referred before, implies the formation of a
254 $\text{Li}_{1-z}\text{Ni}_{1+z}\text{O}_2$ phase in these non-Li-rich compounds since a large amount of the Li was consumed
255 by forming Li_4MoO_5 . As a result, the non-Li-rich phase shows dramatically decreased capacity

256 once more Mo was added, as the $\text{Li}_{1-z}\text{Ni}_{1+z}\text{O}_2$ phase is unfavorable for Li diffusion. Therefore,
 257 these contrasts between Li-rich and non-Li-rich phases further confirm the unique intergrown
 258 structure with LiNiO_2 -rich and Li_4MoO_5 -rich (rather than $\text{Li}_{1-z}\text{Ni}_{1+z}\text{O}_2$) domains for the $\text{Li}_{1+y}\text{Ni}_{(3-5y)/3}\text{Mo}_{2y/3}\text{O}_2$
 259 samples. It can also be inferred that the extra Li added for Li-rich compositions are
 260 mostly electrochemically active or entered into $\text{Li}_{1-z}\text{Ni}_{1+z}\text{O}_2$ lattice to form more
 261 electrochemically active LiNiO_2 domain, rather than stay on the particles surface as Li residues.



262
 263 **Figure 5. Intra-structural change during cycling.** (a)(b) *In situ* XRD pattern (17–21°) for LiNiO_2 and
 264 $\text{Li}_{1.09}\text{Ni}_{0.85}\text{Mo}_{0.06}\text{O}_2$, respectively, during the H2→H3 phase transition. For each compound, left side
 265 shows the pattern evolution while correspondingly, the right side shows the contour plots. Note that the
 266 peak shift looks in a less magnitude in $\text{Li}_{1.09}\text{Ni}_{0.85}\text{Mo}_{0.06}\text{O}_2$ compared with that of LiNiO_2 simply because

267 of the bifurcation in the latter enables more shift of Li-poor phase. (e)(d) Combined SXRD and NPD
268 refinement results for $\text{Li}_{1.09}\text{Ni}_{0.85}\text{Mo}_{0.06}\text{O}_2$ charged to 4.3 V. (e)(f) Combined SXRD and NPD refinement
269 results for $\text{Li}_{1.09}\text{Ni}_{0.85}\text{Mo}_{0.06}\text{O}_2$ discharged to 2.0 V.

270 The benefits of such “Li-rich Ni-rich” combination can be well manifested by the
271 improved electrochemical performances. With increasing Li and Mo contents, the first-cycle
272 Coulombic efficiency increases from 91% to around 98%, with the capacity decreasing first and
273 then increasing to reach even higher values ($>220 \text{ mA h g}^{-1}$) at lower Ni content of 85% and 80%
274 (Fig. 4a). Besides, the $y=0.09$ member $\text{Li}_{1.09}\text{Ni}_{0.85}\text{Mo}_{0.06}\text{O}_2$ shows an excellent capacity retention
275 ($\sim 91\%$) after cycling at 0.1C (20 mA g^{-1}) for 100 cycles at room temperature (Fig. 4c) in stark
276 contrast to that of pure LiNiO_2 ($\sim 64\%$). An 80% capacity retention can also be achieved for
277 $\text{Li}_{1.09}\text{Ni}_{0.85}\text{Mo}_{0.06}\text{O}_2$ cycled at 1C (200 mA g^{-1}) for 260 cycles in a half cell versus Li, while in a
278 full cell versus graphite it can sustain for 350 cycles at 0.5C with 87% retention (Fig. S5). It also
279 shows quite stable cycling curves with negligible voltage decay, as observed from both the
280 galvanostatic cycling and dQ/dV profiles in Fig. 4d. Notably, the plateau of the H2-to-H3 phase
281 transition (shaded region in Fig. 4d), which is known for its detrimental effect to the layered
282 structure, was retained very well upon cycling (Fig. 4d). Besides, while the addition of Li and
283 Mo is supposed to downgrade the electronic conductivity of the compounds, $\text{Li}_{1.09}\text{Ni}_{0.85}\text{Mo}_{0.06}\text{O}_2$
284 shows even slightly better rate performance than that of LiNiO_2 (Fig. S6), seemingly resulting
285 from the smaller LiNiO_2 -rich domains/particles with shorter Li diffusion paths. Moreover, the
286 electrochemical performance of $\text{Li}_{1.09}\text{Ni}_{0.85}\text{Mo}_{0.06}\text{O}_2$ was further investigated in a wider
287 electrochemical window (2.0-4.8V) to pursue higher capacity. Figure S7a indicates that an initial
288 capacity of 250 mA h g^{-1} can be obtained at C/10. Though the capacity fades more quickly, it
289 shows a small voltage hysteresis (energy efficiency: 91%) and negligible voltage decay (Fig.
290 S7b-d), which is far more superior to typical Li-rich NMC cathodes.

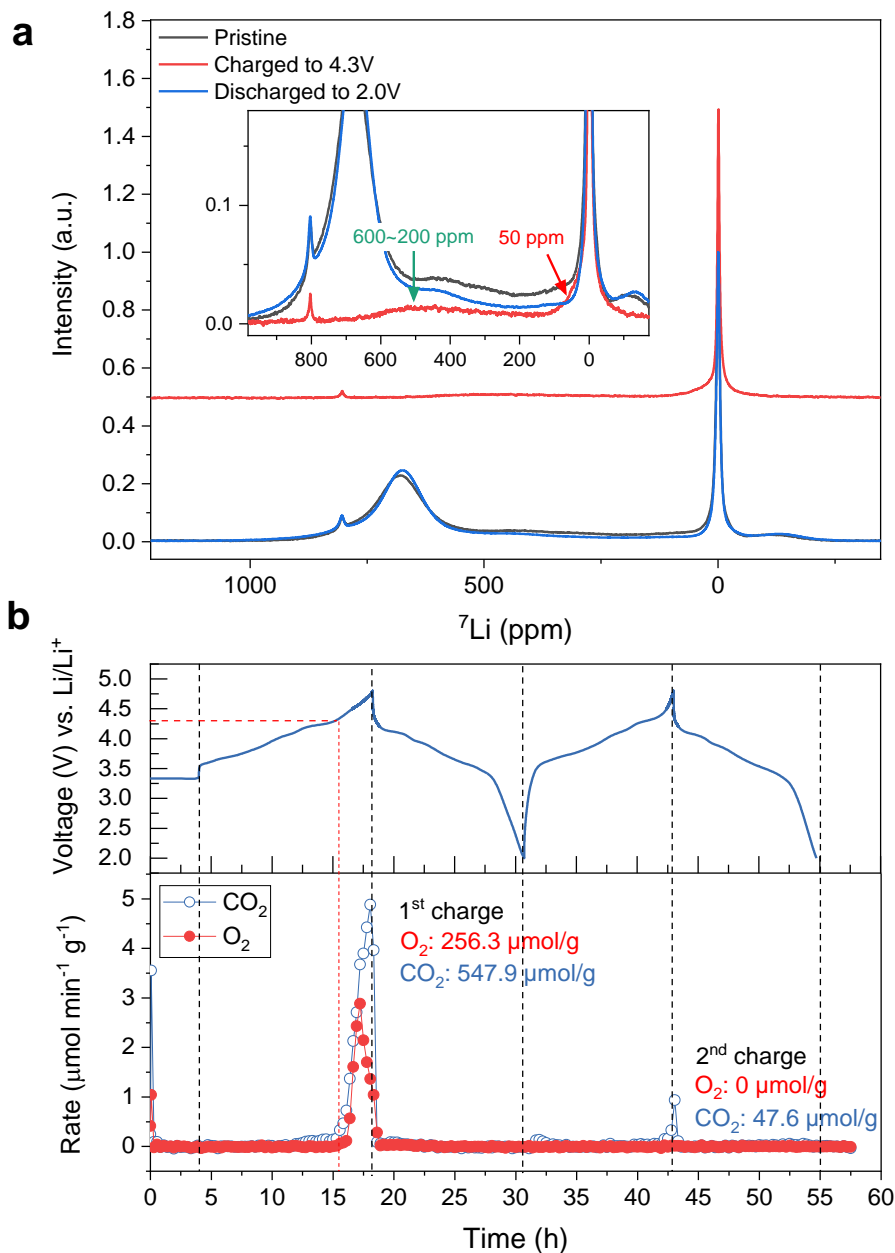
291 Besides, differential scanning calorimetry (DSC) experiments were performed to
292 evaluate the thermal stability of this new family of electrodes (Fig. S8). Two distinctions can be
293 observed between bare LiNiO_2 and $\text{Li}_{1+y}\text{Ni}_{(3-5y)/3}\text{Mo}_{2y/3}\text{O}_2$ ($y=0.09$ and 0.12) samples. First, the
294 main heat flow peak at around 210°C is very sharp and strong for LiNiO_2 , but is much
295 suppressed for Mo-containing samples (Fig. S8). This difference corresponds well to the
296 structural stability improvement of $\text{Li}_{1+y}\text{Ni}_{(3-5y)/3}\text{Mo}_{2y/3}\text{O}_2$ enabled by the intergrown Li_4MoO_5 -
297 rich domains, which might restrain the structural transformation at high temperature and hence
298 the suppressed heat flow. Second, there are additional weak heat flow peaks below 200°C in

299 $\text{Li}_{1+y}\text{Ni}_{(3-5y)/3}\text{Mo}_{2y/3}\text{O}_2$ samples but are absent in LiNiO_2 . Two possibilities can explain these
300 small peaks. One is due to the anionic redox (as will be shown later) aroused in $\text{Li}_{1+y}\text{Ni}_{(3-5y)/3}\text{Mo}_{2y/3}\text{O}_2$
301 that produces more reactive species at high voltage and temperature; second is Mo
302 dissolution might be enhanced at elevated temperature. Both possibilities can be reasonable since,
303 with higher Mo content, the heat release below 200°C is even increased (Fig. S8), consistent
304 with more anionic redox contribution or more Mo dissolution triggered in high Mo-content
305 sample.

306 Further shortcomings of these new class of materials in terms of electrochemical
307 performance should be subjected to discussion. One issue is that $\text{Li}_{1.09}\text{Ni}_{0.85}\text{Mo}_{0.06}\text{O}_2$ shows large
308 voltage hysteresis below 3V (Fig.4a) possibly associated with oxygen redox, as discussed later.
309 Though, the energy efficiency can reach ~95% after initial cycles (Fig. S9), acceptable for
310 practical application. Besides, a lower cutoff voltage down to 2.0V was used for achieving high
311 capacities. However, even by cycling the electrode in 2.7-4.3V vs Li, the voltage window
312 typically employed for Ni-rich materials, a capacity up to 210 mA h g^{-1} can also be obtained with
313 good cycling stability (Fig. S10). Moreover, while limitation do exists for $\text{Li}_{1.09}\text{Ni}_{0.85}\text{Mo}_{0.06}\text{O}_2$
314 when using a high loading (95% active materials, $10\text{-}12 \text{ mg cm}^{-2}$) compared with low loading
315 (80% active material, $6\text{-}8 \text{ mg cm}^{-2}$) as shown in Fig.S11, the performance is highly promising for
316 practical application especially considering it is Co-free.

317 **Structural change.** Since the main active phase in the intergrown structure is LiNiO_2 -
318 rich domain that bears high similarity with pure LiNiO_2 as learnt from TEM, NMR, and
319 electrochemical studies, yet a question lingers why the former shows outstanding
320 electrochemical stability that can hardly be achieved for the latter. First, *in situ* XRD was used to
321 investigate their phase transition behavior during cycling. As shown in Fig. S12a, during the
322 charge process of LiNiO_2 , the (003) diffraction peak undergoes mild changes before reaching 4.2
323 V. However, once reaching the 4.2 V plateau corresponding to the so-called “H2→H3” phase
324 transition, the (003) peak largely shifts towards higher angle (more than 1°), indicative of a large
325 layer spacing shrinkage. Such a “H2→H3” phase transition is also accompanied by a very large
326 local micro-strain as clearly observed from the very asymmetrical peak at the end of charge (Fig.
327 S12c). Besides, in the second cycle, a bifurcation of the (003) peak emerges due to the co-
328 existence of two phases: the Li-rich and Li-poor phases (Fig.5a and Fig. S12c). This
329 phenomenon, previously called as “bulk fatigue” due to the formation of surface disordered rock-

330 salt phase that causes mechanical failure²⁶, is characteristic of some inactive Li ions (in Li-rich
331 phase) that are not electrochemically accessible, hence the fading of the capacity. We also
332 confirmed that this bifurcation behavior happens similarly for regularly synthesized LNiO₂
333 (BASF) in the 2nd cycle but in lesser extent, while it largely aggravates in the 3rd cycle (Fig. S12).
334 By contrast, the (003) peak in Li_{1.09}Ni_{0.85}Mo_{0.06}O₂ shows less shift and less asymmetry during the
335 “H2→H3” phase transition (Fig. S12b). Specially, unlike the case of LiNiO₂, the (003) peak of
336 Li_{1.09}Ni_{0.85}Mo_{0.06}O₂ remains single in the whole “H2→H3” phase transition process (Fig. 5b and
337 Fig.S12d) without any bifurcation. This implies an excellent mechanical reversibility and
338 sustainability of Li_{1.09}Ni_{0.85}Mo_{0.06}O₂ against LiNiO₂, thereby explaining the huge electrochemical
339 stability contrast between these two compounds.



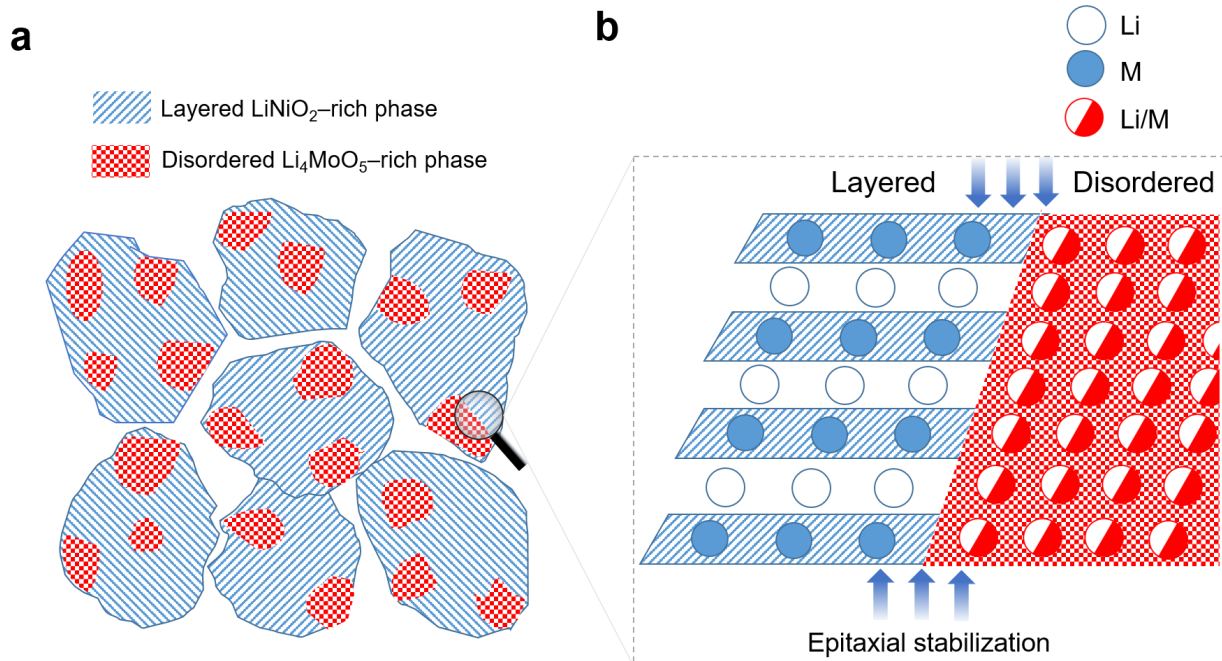
340
 341 **Figure 6. NMR and OEMS study during the cycling of $\text{Li}_{1.09}\text{Ni}_{0.85}\text{Mo}_{0.06}\text{O}_2$.** (a) ^7Li MAS-NMR spectra
 342 of pristine (black), charged (red, top), discharged (blue) $\text{Li}_{1.09}\text{Ni}_{0.85}\text{Mo}_{0.06}\text{O}_2$. Assuming the molybdenum-
 343 rich phase is not active electrochemically, we normalized ^7Li the spectra with respect to the corresponding
 344 peak height at 0 ppm. The inset shows the enlarged view of the overlapped NMR spectra of all three
 345 samples. (b) OEMS result during the first two cycles. A red dashed line marks an onset potential of
 346 slightly above 4.3V for oxygen release at the first cycle. The amounts of O_2 and CO_2 release are indicated.
 347 CO_2 release is generally caused by electrolyte oxidation as previously reported²⁸ and further thoroughly
 348 discussed in Supplementary note II.

349 To further examine the intra-cycle structural change, we performed SXRD, NPD, and
 350 TEM analysis during the first cycle. The SXRD and NPD patterns of $\text{Li}_{1.09}\text{Ni}_{0.85}\text{Mo}_{0.06}\text{O}_2$ in the
 351 charged (4.3 V) and discharged (2.0 V) states were collected and analyzed with Rietveld

352 refinement, as shown in Fig. 5c-f and Table S4-5. The results demonstrate that the long-range
353 cation ordering in $\text{Li}_{1.09}\text{Ni}_{0.85}\text{Mo}_{0.06}\text{O}_2$ is not significantly affected upon cycling, except that a
354 slight deviation of the molar percentage of the Li_4MoO_5 phase is obtained in charged state but
355 which is within the accuracy of quantitative phase analysis by Rietveld method especially
356 considering that the peaks are fully overlapped. Absence of cation migration is also obvious from
357 the HAADF-STEM images of $\text{Li}_{1.09}\text{Ni}_{0.85}\text{Mo}_{0.06}\text{O}_2$ in the charged and discharged states (Fig.
358 S14). The corresponding ED patterns (insets in Fig. S14) indicate the twinned layered O3
359 structure is well retained. To further inspect if local structural variation exists, we collected ^7Li
360 MAS-NMR spectra during the first cycle, as shown in Fig. 6a. Interestingly, we find that, after
361 charge, lithium ions are mostly found in diamagnetic environments (i.e. those that are close to
362 Mo^{6+} ions), except for a very broad component between 600 and 200 ppm (Fig.6a inset, green
363 arrow), and a peak at around 50 ppm (Fig. 6a inset, red arrow) which may be assigned to lithium
364 ions at the interface of the molybdenum-rich phase. After discharge, the LiNiO_2 peak almost
365 fully reemerges except for being slightly sharper, accompanied by a subtle intensity decrease in
366 the range of 20-500 ppm (i.e. Li^+ ions that are close to Mo^{6+}). These results demonstrate that
367 almost all the Li^+ from LiNiO_2 domain can be removed and can reversibly come back whereas
368 the Li ions in Li_4MoO_5 domains are less active. Such good reversible Li intercalation chemistry
369 in LiNiO_2 domain is in line with the high Columbic efficiency observed in $\text{Li}_{1.09}\text{Ni}_{0.85}\text{Mo}_{0.06}\text{O}_2$,
370 hence explaining its comparable capacity with pure LiNiO_2 even with barely active Li_4MoO_5
371 domains in the former. Besides, the online electrochemical mass spectrometry (OEMS)
372 experiment (Fig. 6b) shows an onset potential for oxygen release slightly above 4.3 V at the 1st
373 charge, whereas it is totally absent during the second charge, similar to the previous reports on
374 $\text{LiNi}_{0.8}\text{Co}_{0.1}\text{Mn}_{0.1}\text{O}_2$ ²⁸. Thus, good cycling stability is achieved by cutting off the voltage at 4.3 V,
375 while it severely deteriorates when cycled up to 4.8 V (Fig. S7a). A SXR pattern was also
376 collected after cycling the sample for 50th cycles in the 2.0 - 4.3 V range (Fig. S15), showing
377 excellent retaining of the original structure without noticeable structural disordering, as deduced
378 from the Rietveld refinement (Table S6).

379

380



381

382 **Figure 7.** Schematic of the layered-disordered intergrowth of “Li-rich Ni-rich” cathode. (a) Schematic of
 383 the domains of layered LiNiO_2 -rich phase and disordered Li_4MoO_5 -rich phase in the grains of cathodes.
 384 (b) “Epitaxial stabilization” effect of the intergrowth in reinforcing the mechanical and structural stability
 385 of layered phase in the intergrowth structure.

386 The above these results collectively confirm the benefit of such two-phase intergrowth,
 387 with a Li_4MoO_5 domain sizes in the 5-20 nm range, to the structural and mechanical stability of
 388 Ni-rich oxide due to the “epitaxial stabilization” effect, as schematically shown in Fig. 7. The
 389 superimposition of the diffraction peaks (Fig. 1) of the two phases indicates the similar sub-
 390 lattice parameters and hence the coherent epitaxial interface in between the two domains (Fig. 7).
 391 As a result, the mechanical strain energy during (de)lithiation of LiNiO_2 -rich phase can be
 392 largely counteracted by the epitaxial energy from Li_4MoO_5 domains, thereby decreasing the
 393 deformation and improving the cracking resistance. To simulate such effects, a calculation of
 394 free energy of the two intergrowing crystal with a coherent epitaxial interface is indeed possible
 395 with the DFT-based methods, but it requires precisely known atomic structure and chemical
 396 composition at the interface which we did not investigate in detail in this work. Without these
 397 prerequisites, the simulation results will be too speculative being based on extensive assumptions
 398 not supported by the experimental data. In our interpretation of the role of epitaxial stabilization,
 399 we refer to very recent experimental results demonstrating that epitaxial intergrowth of the
 400 layered oxide cathode material with the disordered RS-type phase helps alleviating strain during
 401 charge/discharge and greatly improve the capacity retention^{29,30}. In addition, by checking further

402 the redox mechanism of $\text{Li}_{1.09}\text{Ni}_{0.85}\text{Mo}_{0.06}\text{O}_2$ via XAS complemented by GITT analysis (Fig.
403 S16), we identified a main Ni redox with a bit contribution from O redox triggered by the slight
404 excess Li in LiNiO_2 -rich phase. A typical signature of anionic redox in this system is the large
405 voltage hysteresis observed below 3 V, which aggravates with increasing Li and Mo contents.
406 Such minor O redox contribution may also plays an role on the cycling stability by buffering the
407 electron depletion of O $2p$ states from Ni($3d$)-O($2p$) σ -type interactions, as we have envisaged at
408 the beginning.

409

410 Discussion.

411 We have explored here a material design strategy by combining the “Li-rich” with the
412 “Ni-rich” concepts together, as shown by the $\text{Li}_{1+y}\text{Ni}_{(3-5y)/3}\text{Mo}_{2y/3}\text{O}_2$ family as a proof of concept.
413 The materials display an intergrowth of a layered LiNiO_2 -rich phase and a disordered Li_4MoO_5 -
414 based domain at the 10 nm scale rather than solid solutions. Such intergrowth of two phases,
415 together with the minor O redox contribution, enables excellent mechanical, structural and
416 cycling stabilities for LiNiO_2 -rich phase, thus expanding the boundary of materials design for
417 practical high-energy-density electrodes.

418 The LiNiO_2 - Li_4MoO_5 intergrowth is reminiscent of previous debates on the real structure
419 of Li-rich NMC ($(1-x)\text{Li}_2\text{MnO}_3 \cdot x\text{LiMO}_2$) compounds on whether they are solid solutions or two-
420 phase (Li_2MnO_3 -rich and LiMO_2 -rich phases) co-existence.³¹⁻³⁶ Similarly, while their XRD
421 patterns exhibit a single-phase feature, local fragments of Li_2MnO_3 can be frequently observed
422 by TEM.^{32,35} An agreement seems to have been achieved that Li-rich NMCs can indeed be
423 considered as solid solutions in the long-range scale but also show some short-range ordering of
424 the two phases. Apparently, the structure of this class of $\text{Li}_{1+y}\text{Ni}_{(3-5y)/3}\text{Mo}_{2y/3}\text{O}_2$ compounds bears
425 the same rationale with Li-rich NMC but with some differences. One is that Mo^{6+} is more
426 insoluble than Mn^{4+} in LiMO_2 layered structures due to its higher valence, hence driving the
427 phase separation of Li_4MoO_5 domains within the LiNiO_2 phase (Fig. 7a). Another is that Mo^{6+} is
428 in d^0 electronic configuration and is more prone to forming disordered rock-salt phase in a Li-
429 rich environment³⁷. Besides, with a 4.3 V cutoff voltage, the Li_4MoO_5 -rich phase in $\text{Li}_{1+y}\text{Ni}_{(3-5y)/3}\text{Mo}_{2y/3}\text{O}_2$
430 compounds is not active, as proven by NMR, unlike Li_2MnO_3 domains in Li-rich

431 NMC charged to 4.8 V, which is crucial to trigger anionic redox and tapping into the associated
432 extra capacity³⁸.

433 Indeed, composite electrode design has been proposed by Thackeray's earlier work in
434 Li_2MnO_3 -based compounds. Several combinations, such as "layered-rocksalt", "layered-layered",
435 "layered-spinel" and so on, were shown to have high capacities and good cycling stabilities.^{39,40}
436 Besides, a "layered-rocksalt" intergrown $\text{Li}_{1.2}\text{Ni}_{0.4}\text{Ru}_{0.4}\text{O}_2$ electrode was also reported recently
437 by N. Li et al.²⁹ While these studies share a similar intergrowth structure, our work, mainly based
438 on the "Li-rich Ni-rich" concept, provides a more practical solution for future cathode design.
439 Besides, several pioneering studies must be mentioned, such as those led by J. Dahn, D. Aurbach,
440 and Y.-K. Sun et al.⁴¹⁻⁴⁴, who attempted to dope $\text{Mo}^{6+}/\text{W}^{6+}$ in LiNiO_2 or its derived Ni-rich
441 compounds, with Mo being infused in grain boundary or segregated in near surface region due to
442 its high insolubility. Hence, our study confirms the Mo^{6+} insolubility they observed, yet it also
443 differs by two aspects: First, in our $\text{Li}_{1+y}\text{Ni}_{(3-5y)/3}\text{Mo}_{2y/3}\text{O}_2$ series, homogenous two-phase
444 intergrowth is achieved, rather than infused boundaries, due to our solution-based synthesis for
445 obtaining a atomically homogeneous precursor. Such an homogeneous two-phase distribution
446 can never been achieved with a simple solid-state synthesis even preceded by a co-precipitation
447 step, as the mass diffusion of Mo^{6+} is difficult and Mo is more prone to precipitating in acidic
448 solution, therefore making it impossible to co-precipitate synchronously with Ni in alkaline
449 solution. Second, Li excess is essential to ensure the two-phase structure and the associated
450 performance as already implied by our previous control studies (Fig. S4).

451 Finally, our conceptualization of "Li-rich Ni-rich" compounds can further expand the
452 space of high-energy cathode materials design, since Mo^{6+} can be replaced by other high-valence
453 transition metal or metalloid ions, such as W^{6+} , Te^{6+} , V^{5+} , Nb^{5+} , Sb^{5+} , Ta^{5+} , Ti^{4+} , Mn^{4+} , or Zr^{4+}
454 etc. A preliminary study has been implemented on Ti^{4+} and Nb^{5+} systems as the representatives
455 of tetravalent and pentavalent transition metal ion doping, showing high resemblance to the case
456 of $\text{Li}_{1+y}\text{Ni}_{(3-5y)/3}\text{Mo}_{2y/3}\text{O}_2$ (Fig. S17). Notwithstanding, some practical parameters of these newly
457 designed electrodes remains to be improved, such as the slightly lower tap density ($1.96(3)\text{g}\cdot\text{cm}^{-3}$)
458 due to the smaller particle size. Future works can focus on seeking better, more abundant,
459 high-valence M ions or combinations of those to further enhance the electrode properties. This
460 has to be done by intensively scrutinizing the ternary composition-structure-electrochemistry
461 relationships of these potential "Li-rich Ni-rich" materials. Besides, the impact of the synthetic

462 method on the microstructure at the nanometer scale and their effect on performances of the
463 electrode remains to be further explored in pursuit of higher practicability. On solving these
464 problems, we believe this study will pave a new way to access practical high-energy-density
465 cathodes for Li-ion batteries.

466

467 **Experimental**

468 **Materials synthesis**

469 $\text{Li}_{1+y}\text{Ni}_{(3-5y)/3}\text{Mo}_{2y/3}\text{O}_2$ ($y=0, 0.03, 0.06, 0.09, 0.12$) and $\text{LiNi}_{1-y}\text{Mo}_y\text{O}_2$ ($y=0.02, 0.04, 0.06, 0.8$) were
470 prepared by a solid-state process preceded by a solution step to obtain the precursors. To prepare the
471 precursors, stoichiometric amounts of lithium acetate dihydrate (2% excess, reagent grade, Sigma-
472 Aldrich), nickel(II) acetate tetrahydrate ($\geq 99.0\%$ (KT), Sigma-Aldrich) and $(\text{NH}_4)_6\text{Mo}_7\text{O}_{24}\cdot 4\text{H}_2\text{O}$ (ACS,
473 81-83% as MoO_3) were dissolved in water or ethanol, followed by drying the solution to form a viscous
474 gel. The gel was then dried at 120°C in air for at least 8 hours, and hand ground before high-temperature
475 annealing at 750°C under oxygen flow for 8 hours, followed by reannealing in the same condition (750°C ,
476 8h, O_2 flow). Note that a low amount of target compound (~ 0.5 g) is easier to obtain phase-pure, whereas
477 scaling up will sometimes lead to easily detected impurities (mainly Li_4MoO_5), as observed from XRD.

478 **Electrochemistry**

479 Electrochemical studies were done in 2032-type coin cells unless otherwise specified. 80 wt.% of active
480 materials with 20 wt.% carbon (Super P) were homogeneously mixed together as cathode electrodes. The
481 coin cells were assembled with the cathode powder (with a loading of $6\text{-}8\text{ mg/cm}^2$) countered by a Li foil
482 as the anode, between which two Whatman GF/D borosilicate glass fiber sheets were used as the
483 separator. LP 57 electrolyte (1M LiPF_6 in EC/EMC= 30:70 wt.%) mixed with 2 wt.% vinylene carbonate
484 (VC) was used as electrolyte for cycling between 2.0 and 4.3 V, whereas a LP30 electrolyte (1M LiPF_6 in
485 EC/DMC= 50:50 wt.%, E-Lyte) was used for cycling between 2.0 and 4.8 V.

486 **General characterization (ICP, XRD, NPD, SEM and DSC).**

487 The ICP-AES data was collected with a PerkinElmer NexION 2000 ICP mass spectrometer, and the
488 samples were first dissolved with *aqua regia* and then adjusted to appropriate concentrations with
489 deionized water in a volumetric flask before the measurements. XRD patterns were obtained via a
490 laboratory X-ray diffractometer (BRUKER D8 Advance) equipped with a Cu $\text{K}\alpha$ radiation source ($\lambda_{\text{K}\alpha 1} =$
491 1.54056 \AA , $\lambda_{\text{K}\alpha 2} = 1.54439\text{ \AA}$) and a Lynxeye XE detector. A homemade airtight cell with a beryllium
492 window was used for *in situ* XRD experiments, for which the electrochemistry was ran synchronously
493 with data acquisition. Constant-wavelength NPD data were collected at room temperature on the
494 WOMBAT high intensity neutron powder diffractometers, with the sample sealed under Argon, using a
495 wavelength of 1.6215 \AA . All the Rietveld refinements of the XRD and NPD patterns were done with the
496 FullProf program⁴⁵. SEM images were obtained on an FEI Magellan scanning electron microscope
497 equipped with an Oxford Instruments energy dispersive X-ray spectroscopy (EDX) detector. EDX was
498 carried out using an acceleration voltage of 20 kV. DSC experiments were carried out with a Mettler
499 Toledo TGA/DSC 3+ (LF 1100 °C) equipment at a rate of $5\text{ }^\circ\text{C min}^{-1}$ between 25 and $300\text{ }^\circ\text{C}$ under a
500 constant Ar gas flow. The samples for DSC were charge to 4.3 V and recovered, washed by DMC for
501 three times, and then dried under vacuum. The tests were conducted by soaking the 3~5 mg dried samples
502 into 100 μl LP57 electrolyte and sealed in an aluminum crucible.

503

504 **TEM**

505 Samples for transmission electron microscopy (TEM) were prepared in an Ar-filled glovebox by grinding
506 the powders in an agate mortar in dimethyl carbonate and depositing drops of suspension onto copper
507 TEM grid with holey carbon support layer. The sample was transported to the TEM column by means of
508 a Gatan vacuum transfer holder completely avoiding contact with air and moisture. Electron diffraction
509 (ED) patterns, high angle annular dark field scanning transmission electron microscopy (HAADF-STEM)
510 images and energy-dispersive X-ray (EDX) spectra were collected with a probe-corrected Titan Themis Z
511 electron microscope operated at 200 kV and equipped with a Super-X EDX detector.

512 **OEMS**

513 Freestanding electrodes comprised 70% wt. active materials, 20% wt. carbon (Super P) and 10% PTFE
514 were used. An in-house designed OEMS cell⁴⁶ was used to run the experiment. 150 μ L of LP30
515 electrolyte, Li foil as anode and 1 piece of GF/D glassfiber separator were used to assemble the half-cell.
516 The quantitative gas evolution data on m/z channels of 32 (O_2) and 44 (CO_2) was collected using an
517 *operando* protocol where the cell was rested for 4 h before and 12 h after the full electrochemistry cycle
518 to stabilize the background signal. The OEMS cells were cycled in the 2.0 - 4.8 V range for two cycles at
519 a C/10 rate (20 mA g^{-1}). At least two cells were tested to ensure results reproducibility.

520 **XAS**

521 Ni K-edge and Mo K-edge XAS spectra were collected in transmission mode at ROCK⁴⁷ beamline of the
522 SOLEIL synchrotron facility at Paris, France. A Si(111) channel-cut quick-XAS monochromator with an
523 energy resolution of 0.7 eV at 7 keV was used. The intensity of the monochromatic X-ray beam was
524 measured using three consecutive ionization detectors. For sample preparation, powders (80% active
525 material and 20% carbon super P) were cycled to specific states of charge and then recovered, washed
526 with DMC for three times, and finally dried under reduced pressure. Then the dried powders were mixed
527 with certain amount of cellulose, and pressed as thin pellets. The pellets were sealed carefully into X-ray
528 transparent plastic bags before taking to XAS measurements. The energy calibration was performed using
529 Ni and Mo foils placed between the second and third ionization chambers. All XAS data were processed
530 with the Athena program⁴⁸.

531 **NMR**

532 Solid-state NMR experiments were performed on a 4.7 T Avance III HD Bruker NMR spectrometer (200
533 MHz for 1H , 77.8 MHz for 7Li , 29.4 MHz for 6Li), using a 1.3 mm magic angle spinning (MAS) probe
534 spinning at 62.5 kHz under pure nitrogen gas. Without temperature regulation, the temperature inside the
535 rotor is expected to be around 50°C. All 7Li NMR experiments were recorded with a rotor-synchronized
536 Hahn echo sequence, and the 90° pulse was set to 1.1 μ s and the chemical shift was referenced with liquid
537 7LiCl in water at 0 ppm (corresponding to a 227 kHz B_1 field strength). The T_1 relaxation times were
538 measured using a saturation-recovery experiment, using 20 x 90° pulses separated by a 1 ms delay for
539 saturation. The T_1 behavior was found to be mono-exponential for the left hand side peaks (around 600-
540 850 ppm) and the T_1 values were around 2-5 ms, as expected for 7Li spins close to paramagnetic Ni^{3+} ions.
541 For the diamagnetic part, the T_1 relaxation was found to be multiexponential, with at least two
542 components, a slow relaxing component with T_1 values between 1 and 1.5 seconds, while a fast relaxing
543 component was observed with T_1 values between 5 and 30ms. This is expected as, first, the spinning
544 sideband from the $LiNiO_2$ peak overlaps with the 0 ppm contribution (fitted in red, on the right hand side,
545 around -120 ppm); second, the diamagnetic contribution is made of lithium in molybdenum-rich domains,
546 embedded in the $LiNiO_2$ phase, and therefore, lithium ions close to the interface will display shorter
547 relaxation times. Therefore, all 7Li spectra were recorded using a 5 to 10 s relaxation delays to ensure a

548 proper quantification of the diamagnetic contribution, with at least 1024 transients recorded to ensure a
549 sufficient signal-to-noise ratio. The ${}^6\text{Li}$ Hahn echo experiment was obtained with a 90° pulse of $2.1\ \mu\text{s}$
550 duration, and a 50 ms recovery delay was used, allowing for the recovery of the magnetization of the ${}^6\text{Li}$
551 close to Ni ions. However, the experiment is not quantitative for the slow relaxing ${}^6\text{Li}$ spins in the
552 diamagnetic phase, and 675,504 transients were recorded to obtain a good signal-to-noise ratio. The ${}^6\text{Li}$
553 NMR spectrum was recorded to confirm that not peak was overlapping with the spinning sidebands that
554 are observed in the ${}^7\text{Li}$ spectrum, as shown in [Figure S18](#). The spectra were deconvoluted with dmfit,
555 using the minimum number of necessary Gausso-Lorentzian spinning sideband patterns (5 spinning
556 sidebands maximum) characterized by a Gaussian/Lorentzian ratio, a position (in ppm), a width (in ppm),
557 and an intensity, all of which were fitted by the program.⁴⁹ The spinning sidebands intensities were fitted
558 (no model was used) independently, and the relative weight of each contribution was obtained from the
559 area of the whole spinning sideband pattern. Special care was taken to measure NMR spectra on fresh
560 samples with as little contact as possible with residual moisture in the glovebox or in the NMR
561 spectrometer.

564 **ACKNOWLEDGMENTS**

565 This research used resources of the Advanced Photon Source, a US Department of Energy (DOE)
566 Office of Science User Facility, operated for the DOE Office of Science by Argonne National
567 Laboratory under Contract No. DE-AC02-06CH11357. We are grateful to Tuncay Koç for his
568 kind help in performing SEM and EDX measurements, to Valentin Meunier and Ivette Aguilar
569 for their kind help in measuring ICP, to Antonella Iadecola for her help in collecting the XAS
570 spectra, and to Sathiya Mariyappan for her kind help in performing the DSC measurements.
571 A.M.A. is grateful to the Russian Science Foundation for financial support (grant 20-13-00233).
572 Access to TEM facilities was granted by the Advance Imaging Core Facility of Skoltech. J.-M.T
573 and B.L. acknowledge funding from the European Research Council (ERC) (FP/2014)/ERC
574 Grant-Project 670116-ARPEMA.

576 **AUTHOR CONTRIBUTIONS**

577 B.L. and J.-M.T. conceived the idea and designed the experiments. B.L. carried out the synthesis,
578 structural characterization and electrochemical analysis. G.R. did the analysis of SXRD and NPD
579 data. M.A. collected the NPD patterns. A.M.A. performed TEM experiments and did the analysis.
580 L.Z. did the OEMS experiments and data analysis. M.D. collected NMR data and did the
581 analysis. B.L. and J.-M.T. wrote the manuscript with the contributions from all the authors.

582

583 DECLARATION OF INTERESTS

584 The “Li-rich Ni-rich” materials are patented by Collège de France and Umicore (inventors B.L.
585 and J.-M.T.) with patent application number A22012-EP-EPA and A22012-EP-EPA2 (pending).

586

587

588 REFERENCES

589

590 1. IEA (2020), Global EV Outlook 2020, IEA, Paris [https://www.iea.org/reports/global-ev-outlook-](https://www.iea.org/reports/global-ev-outlook-2020)
591 [2020](https://www.iea.org/reports/global-ev-outlook-2020).

592 2. M. S. Whittingham, *Chemical Reviews*, 2004, **104**, 4271-4302.

593 3. P. Rozier and J. M. Tarascon, *Journal of The Electrochemical Society*, 2015, **162**, A2490-A2499.

594 4. G. Assat and J.-M. Tarascon, *Nature Energy*, 2018, **3**, 373-386.

595 5. B. Li and D. Xia, *Advanced materials*, 2017, **29**.

596 6. M. Zhang, D. A. Kitchaev, Z. Lebens-Higgins, J. Vinckeviciute, M. Zuba, P. J. Reeves, C. P.
597 Grey, M. S. Whittingham, L. F. J. Piper, A. Van der Ven and Y. S. Meng, *Nature Reviews*
598 *Materials*, 2022.

599 7. M. Li, T. Liu, X. Bi, Z. Chen, K. Amine, C. Zhong and J. Lu, *Chem Soc Rev*, 2020, **49**, 1688-
600 1705.

601 8. B. Li and J.-M. Tarascon, 2022.

602 9. S.-T. Myung, F. Maglia, K.-J. Park, C. S. Yoon, P. Lamp, S.-J. Kim and Y.-K. Sun, *ACS Energy*
603 *Letters*, 2017, **2**, 196-223.

604 10. W. Li, E. M. Erickson and A. Manthiram, *Nature Energy*, 2020, **5**, 26-34.

605 11. S. S. Zhang, *Energy Storage Materials*, 2020, **24**, 247-254.

606 12. J. Liu, Z. Du, X. Wang, S. Tan, X. Wu, L. Geng, B. Song, P.-H. Chien, S. M. Everett and E. Hu,
607 *Energy & Environmental Science*, 2021.

608 13. A. O. Kondrakov, H. Geßwein, K. Galdina, L. de Biasi, V. Meded, E. O. Filatova, G.
609 Schumacher, W. Wenzel, P. Hartmann, T. Brezesinski and J. Janek, *The Journal of Physical*
610 *Chemistry C*, 2017, **121**, 24381-24388.

611 14. M. Dixit, B. Markovsky, F. Schipper, D. Aurbach and D. T. Major, *The Journal of Physical*
612 *Chemistry C*, 2017, **121**, 22628-22636.

613 15. H. H. Sun, U.-H. Kim, J.-H. Park, S.-W. Park, D.-H. Seo, A. Heller, C. B. Mullins, C. S. Yoon
614 and Y.-K. Sun, *Nature Communications*, 2021, **12**, 6552.

615 16. C.-H. Jung, Q. Li, D.-H. Kim, D. Eum, D. Ko, J. Choi, J. Lee, K.-H. Kim, K. Kang, W. Yang and
616 S.-H. Hong, *Journal of Materials Chemistry A*, 2021, **9**, 17415-17424.

617 17. C. Zhang, J. Wan, Y. Li, S. Zheng, K. Zhou, D. Wang, D. Wang, C. Hong, Z. Gong and Y. Yang,
618 *Journal of Materials Chemistry A*, 2020, **8**, 6893-6901.

619 18. T. P. Dadze, G. A. Kashirtseva, M. P. Novikov and A. V. Plyasunov, *Fluid Phase Equilibria*,
620 2017, **440**, 64-76.

621 19. M. Bianchini, M. Roca-Ayats, P. Hartmann, T. Brezesinski and J. Janek, *Angewandte Chemie*,
622 2019, **58**, 10434-10458.

623 20. C. Marichal, J. Hirschinger, P. Granger, M. Menetrier, A. Rougier and C. Delmas, *Inorganic*
624 *Chemistry*, 1995, **34**, 1773-1778.

625 21. C. Chazel, M. Ménétrier, L. Croguennec and C. Delmas, *Magnetic Resonance in Chemistry*, 2005,
626 **43**, 849-857.

627 22. D. Carlier, M. Ménétrier, C. P. Grey, C. Delmas and G. Ceder, *Physical Review B*, 2003, **67**,
628 174103.

- 629 23. D. Zeng, J. Cabana, J. Bréger, W.-S. Yoon and C. P. Grey, *Chemistry of Materials*, 2007, **19**,
630 6277-6289.
- 631 24. C. Chazel, M. Ménétrier, L. Croguennec and C. Delmas, *Inorganic Chemistry*, 2006, **45**, 1184-
632 1191.
- 633 25. H. Li, W. Hua, X. Liu-Théato, Q. Fu, M. Desmau, A. Missyul, M. Knapp, H. Ehrenberg and S.
634 Indris, *Chemistry of Materials*, 2021, **33**, 9546-9559.
- 635 26. C. Xu, K. Marker, J. Lee, A. Mahadevegowda, P. J. Reeves, S. J. Day, M. F. Groh, S. P. Emge, C.
636 Ducati, B. Layla Mehdi, C. C. Tang and C. P. Grey, *Nature materials*, 2021, **20**, 84-92.
- 637 27. N. Zhang, J. Li, H. Li, A. Liu, Q. Huang, L. Ma, Y. Li and J. R. Dahn, *Chemistry of Materials*,
638 2018, **30**, 8852-8860.
- 639 28. D. Streich, C. Erk, A. Guéguen, P. Müller, F.-F. Chesneau and E. J. Berg, *The Journal of*
640 *Physical Chemistry C*, 2017, **121**, 13481-13486.
- 641 29. N. Li, M. Sun, W. H. Kan, Z. Zhuo, S. Hwang, S. E. Renfrew, M. Avdeev, A. Huq, B. D.
642 McCloskey, D. Su, W. Yang and W. Tong, *Nature Communications*, 2021, **12**, 2348.
- 643 30. D. P. Singh, Y. A. Birkhölzer, D. M. Cunha, T. Dubbelink, S. Huang, T. A. Hendriks, C. Lievens
644 and M. Huijben, *ACS Applied Energy Materials*, 2021, **4**, 5024-5033.
- 645 31. H. Yu, R. Ishikawa, Y. G. So, N. Shibata, T. Kudo, H. Zhou and Y. Ikuhara, *Angewandte Chemie*,
646 2013, **52**, 5969-5973.
- 647 32. Z. Lu, L. Y. Beaulieu, R. A. Donaberger, C. L. Thomas and J. R. Dahn, *Journal of The*
648 *Electrochemical Society*, 2002, **149**, A778.
- 649 33. K. A. Jarvis, Z. Deng, L. F. Allard, A. Manthiram and P. J. Ferreira, *Chemistry of Materials*, 2011,
650 **23**, 3614-3621.
- 651 34. S. H. Kang, P. Kempgens, S. Greenbaum, A. J. Kropf, K. Amine and M. M. Thackeray, *Journal*
652 *of Materials Chemistry*, 2007, **17**, 2069-2077.
- 653 35. C. H. Lei, J. Bareño, J. G. Wen, I. Petrov, S. H. Kang and D. P. Abraham, *Journal of Power*
654 *Sources*, 2008, **178**, 422-433.
- 655 36. D. Mohanty, A. Huq, E. A. Payzant, A. S. Sefat, J. Li, D. P. Abraham, D. L. Wood and C. Daniel,
656 *Chemistry of Materials*, 2013, **25**, 4064-4070.
- 657 37. A. Urban, A. Abdellahi, S. Dacek, N. Artrith and G. Ceder, *Phys Rev Lett*, 2017, **119**, 176402.
- 658 38. G. Assat, D. Foix, C. Delacourt, A. Iadecola, R. Dedryvere and J. M. Tarascon, *Nat Commun*,
659 2017, **8**, 2219.
- 660 39. J. R. Croy, S. H. Kang, M. Balasubramanian and M. M. Thackeray, *Electrochemistry*
661 *Communications*, 2011, **13**, 1063-1066.
- 662 40. M. M. Thackeray, C. S. Johnson, J. T. Vaughey, N. Li and S. A. Hackney, *Journal of Materials*
663 *Chemistry*, 2005, **15**, 2257-2267.
- 664 41. U. H. Kim, D. W. Jun, K. J. Park, Q. Zhang, P. Kaghazchi, D. Aurbach, D. T. Major, G. Goobes,
665 M. Dixit, N. Leifer, C. M. Wang, P. Yan, D. Ahn, K. H. Kim, C. S. Yoon and Y. K. Sun, *Energy*
666 *& Environmental Science*, 2018, **11**, 1271-1279.
- 667 42. C. Geng, D. Rathore, D. Heino, N. Zhang, I. Hamam, N. Zaker, G. A. Botton, R. Omessi, N.
668 Phattharasupakun, T. Bond, C. Yang and J. R. Dahn, *Advanced Energy Materials*, 2021, 2103067.
- 669 43. G.-T. Park, D. R. Yoon, U.-H. Kim, B. Namkoong, J. Lee, M. M. Wang, A. C. Lee, X. W. Gu, W.
670 C. Chueh, C. S. Yoon and Y.-K. Sun, *Energy & Environmental Science*, 2021, **14**, 6616-6626.
- 671 44. D. Rathore, C. Geng, N. Zaker, I. Hamam, Y. Liu, P. Xiao, G. A. Botton, J. Dahn and C. Yang,
672 *Journal of The Electrochemical Society*, 2021, **168**, 120514.
- 673 45. J. Rodríguez-Carvajal, *Physica B: Condensed Matter*, 1993, **192**, 55-69.
- 674 46. L. Zhang, C. Tsolakidou, S. Mariyappan, J.-M. Tarascon and S. Trabesinger, *Energy Storage*
675 *Materials*, 2021, **42**, 12-21.
- 676 47. V. Briois, C. La Fontaine, S. Belin, L. Barthe, T. Moreno, V. Pinty, A. Carcy, R. Girardot and E.
677 Fonda, *Journal of Physics: Conference Series*, 2016, **712**, 012149.
- 678 48. B. Ravel and M. Newville, *Journal of Synchrotron Radiation*, 2005, **12**, 537-541.

679 49. D. Massiot, F. Fayon, M. Capron, I. King, S. Le Calvé, B. Alonso, J.-O. Durand, B. Bujoli, Z.
680 Gan and G. Hoatson, *Magnetic Resonance in Chemistry*, 2002, **40**, 70-76.